# Shock-adiabatic to quasi-isentropic compression of warm dense helium up to 150 GPa

J. Zheng, Q. F. Chen,* Y. J. Gu, J. T. Li, Z. G. Li, C. J. Li, and Z. Y. Chen

*Laboratory of Shock Wave and Detonation Physics, Institute of Fluid Physics, P.O. Box 919-102, Mianyang, Sichuan, P. R. China*

(Received 18 January 2017; revised manuscript received 26 May 2017; published 20 June 2017)

Multiple reverberation compression can achieve higher pressure, higher temperature, but lower entropy. It is available to provide an important validation for the elaborate and wider planetary models and simulate the inertial confinement fusion capsule implosion process. In the work, we have developed the thermodynamic and optical properties of helium from shock-adiabatic to quasi-isentropic compression by means of a multiple reverberation technique. By this technique, the initial dense gaseous helium was compressed to high pressure and high temperature and entered the warm dense matter (WDM) region. The experimental equation of state (EOS) of WDM helium in the pressure-density-temperature ($P$-$\rho$-$T$) range of 1–150 GPa, 0.1–1.1 g cm$^{-3}$, and 4600–24 000 K were measured. The optical radiations emanating from the WDM helium were recorded, and the particle velocity profiles detecting from the sample/window interface were obtained successfully up to 10 times compression. The optical radiation results imply that dense He has become rather opaque after the 2nd compression with a density of about 0.3 g cm$^{-3}$ and a temperature of about 1 eV. The opaque states of helium under multiple compression were analyzed by the particle velocity measurements. The multiple compression technique could efficiently enhanced the density and the compressibility, and our multiple compression ratios ($\eta_i = \rho_i/\rho_0$, $i$ = 1–10) of helium are greatly improved from 3.5 to 43 based on initial precompressed density ($\rho_0$). For the relative compression ratio ($\eta_i' = \rho_i/\rho_{i-1}$), it increases with pressure in the lower density regime and reversely decreases in the higher density regime, and a turning point occurs at the 3rd and 4th compression states under the different loading conditions. This nonmonotonic evolution of the compression is controlled by two factors, where the excitation of internal degrees of freedom results in the increasing compressibility and the repulsive interactions between the particles results in the decreasing compressibility at the onset of electron excitation and ionization. In the $P$-$\rho$-$T$ contour with the experiments and the calculations, our multiple compression states from insulating to semiconducting fluid (from transparent to opaque fluid) are illustrated. Our results give an elaborate validation of EOS models and have applications for planetary and stellar opaque atmospheres.

DOI: 10.1103/PhysRevB.95.224104

## I. INTRODUCTION

Warm dense matter (WDM) has played an important role in the planetary and stellar evolvement of astrophysics [1–3], the interior structure of the earth [4,5], and processing of the inertial confinement fusion (ICF) action [6]. It prompts the development of the experiments and theories of WDM [7–9], especially for noble gas helium (He), widely existing in the universe. Until now, the thermodynamics [10–12], opacity [13,14], and conductivity [14,15] of He have been studied. The experimental equation of state (EOS) in a pressure range of 2 Mbar has been performed by combining the laser with a diamond-anvil-cell precompression technique [11,12]. By this technique, the reflectivity of dense fluid He was measured by an optical method, which would deduce the electronic conduction results [13]. By means of high explosives, dense gaseous He was quasi-isentropically compressed up to 50 Mbar [16], but the pressure was determined by the calculation. Several theoretical models from Saumon-Chabrier-Van Horn (SCVH) [17], activity expansion (ACTEX) [18], density functional theory (DFT) [19], and path-integral Monte Carlo (PIMC) [19] have predicted rather a discrepancy of compressibility at the onset of ionization in warm dense regimes, where He is strongly coupled, mostly degenerate, and nonideal. This resulted in the controversy about the interior structure and evolution of the giant planet, such as the hydrogen-helium demixing and the cooling time of Saturn and Jupiter [20,21]. The key factor is that available experimental data with higher precision are very limited and urgently required to constrain the EOS model.

The phase transition of fluid He such as metallization and plasma phase transition (PPT) is an open question. An earlier free-energy model predicted that a first-order PPT from neutral atom to singly charged ion would happen in a density range of ∼2.5 g cm$^{-3}$ [22]. The nonmetal-to-metal (insulator-to-conducting) transition of fluid He at about 1 g cm$^{-3}$ was found by electrical conductivity measurements [15] and quantum molecular dynamics (QMD) calculations [23], while the reflectivity measurements with mobility gas closure predicted that dense He became metallic at above ∼1.9 g cm$^{-3}$ [13], maybe at much higher density of around 10 g cm$^{-3}$ [9]. The metallization densities of He are unexpectedly lower or higher than the PPT state by the free-energy model. Taking into account the lack of the polarization interactions and the corrections to the ionization energy in the earlier free-energy model, the calculated PPT state might be debatable and there is no experimental evidence for the existence of the PPT in helium.

In current work, we employ the multiple reverberation compression to generate WDM He from a shock-adiabatic to a quasi-isentropic path. This successive course is very useful to increase the compressibility and reduce the entropy change. By means of the optical diagnostics, the integrated EOS results of WDM He were determined in the pressure-density-temperature range up to ∼150 GPa, ∼1.1 g cm$^{-3}$, and ∼24 kK from 1st to 10th compression, and the multiple compressibility has been discussed. The optical radiance

*chenqf01@gmail.com

 

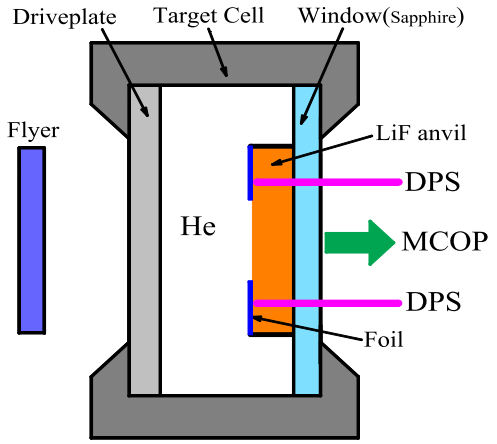


FIG. 1. Sketch of the experimental target and diagnostic devices for warm dense He (drawing not to scale).

measurement implies that dense He has become rather opaque after the 2nd compression. This opaque phenomenon would appear in an amorphous semiconductor with the electrons of low mobility, rather than free electrons [14]. The opacity of He has a reference value for white dwarf stars with unexpectedly opaque He atmospheres.

## II. EXPERIMENTS AND DATA ANALYSIS

A sketch of the experimental target is shown in Fig. 1. Before the experiment, a gaseous helium sample is initially precompressed to 20–40 MPa at room temperature, which is enclosed within the sandwich structure between a driveplate ahead (304 stainless steel, ~5.0 mm thick) and a window back (sapphire, ~2.0 mm thick). Before the window, an anvil (lithium fluoride, LiF, ~4.0 mm thick) with a glued foil (aluminum, ~0.13 mm thick) is used for the interface particle velocity measurement. This thickness of the foil is non-negligible in the data processing. The central area of the foil is hollow to transmit the optical radiance of shocked He. The similar multicompressed target has been shown in our previous work for argon [24], where the double-layer LiF is used to protect the foil from thermal ablation. Compared with argon, the current specimen of He should be shocked to lower temperature, and it is not sufficient to ablate the foil. In addition, the design with a single-layer LiF anvil can efficiently avoid the influence of a catch-up wave under multicompression. Also, the distortion of the driveplate in the precompressed states was recorded by a displacement-measuring instrument.

By means of a two-stage light gas-gun facility, the flyer (tantalum, ~3.2 mm thick and ~28 mm diameter) is accelerated to impact the driveplate, and then the shock wave is generated and transmits into the sample of He. The shock wave in He will propagate and reverberate repeatedly between the driveplate and the anvil due to the higher shock impedance. Compared with the laser and magnetically driven facility, the gas gun could accelerate a large-scale flyer and avoid the influence of rarefaction and catch-up waves under multicompression EOS measurement. Usually, the ratio of the diameter to the thickness is larger than 2. Under multiple shock compression, the transmission time in the He chamber is longer and this

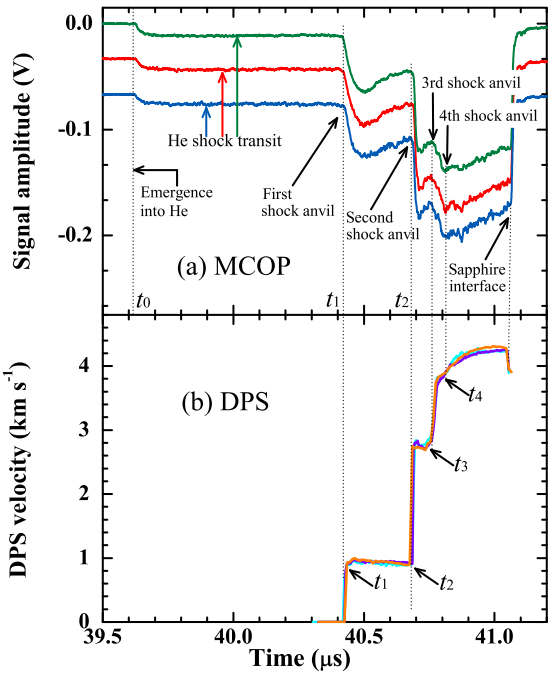


FIG. 2. Typical experimental signals of multiple compressed He for the shot of No. GHe-6: (a) the spectral radiance history from MCOP and (b) the interface particle velocity history from DPS.

ratio should be much larger. Throughout all the diagnostic signals the edge release waves do not affect the experimental results. By the reverberating technique, the He gas would be multicompressed into a warm dense regime.

The EOS of warm dense He was obtained by measured the spectral radiance history from a multichannel optical pyrometer (MCOP) [25] and the interface particle velocity history from a Doppler-pins system (DPS) [26] shown in Figs. 2(a) and 2(b) for the shot of GHe-6. When the shock wave entered and passed through the He sample chamber for the first time, the nearly flat regime (between $t_0$ and $t_1$) indicates that the shock-compressed He with good uniformity was generated. The 1st shock velocity ($U_{s1}$) was directly obtained from the crossing time and the He chamber thickness, where the distortion of the chamber thickness was recorded by a displacement-measuring instrument in the current precompressed state. The 1st pressure ($P_1$) and density ($\rho_1$) of He were determined by the impedance matching method [24] to solve the Rankine-Hugoniot equations. The material Hugoniot parameters [27] for our experimental target were used.

Subsequently, when the shock impacted the LiF anvil, firstly ($t_1$) a reflected shock wave was generated back to the He sample and a transmitted shock wave entered the LiF anvil simultaneously. The sample was reshocked to a state with higher density and temperature, which leads to an abrupt increase of optical radiance intensity from He. This increasing radiance is observed from the 2nd step signal of MCOP shown in Fig. 2(a). Along with the optical absorption of the compressed He sample, the 2nd step intensity would decrease gradually. Until the shock reverberated and impacted the LiF for the second time ($t_2$), the 2nd step (between $t_1$ and $t_2$) shows the process including the 2nd and 3rd shock-compressed He. Therefore, the 2nd and the following multiple

TABLE I. Single-shock velocities ($U_{s,1}$) of He measured by MCOP and multishock particle velocities ($U_{pi,LiF}$, $i = 1,2,3,4,5$) of LiF measured by DPS. The initial density ($\rho_0$) is measured by a method of draining with a pressure vessel with the initial pressure ($P_0$) at room temperature. The uncertainty of $U_{S,1}$ is determined by the He chamber thickness and the crossing time uncertainty. The uncertainties of $U_{pi,LiF}$ are determined by the DPS uncertainty and the multiple channels average uncertainty. $W$ is the flyer impact velocity.

| Shot No. | $P_0$ (MPa) | $\rho_0$ (g cm$^{-3}$) | $W$ (km s$^{-1}$) | $U_{s,1}$ (km s$^{-1}$) | $U_{p1,LiF}$ (km s$^{-1}$) | $U_{p2,LiF}$ (km s$^{-1}$) | $U_{p3,LiF}$ (km s$^{-1}$) | $U_{p4,LiF}$ (km s$^{-1}$) | $U_{p5,LiF}$ (km s$^{-1}$) |
|---|---|---|---|---|---|---|---|---|---|
| GHe-1 | $20.5 \pm 0.1$ | $0.030 \pm 0.001$ | $5.024 \pm 0.025$ | $8.29 \pm 0.03$ | $0.51 \pm 0.01$ | $1.92 \pm 0.02$ | $3.20 \pm 0.03$ | $3.69 \pm 0.04$ | $3.92 \pm 0.04$ |
| GHe-2 | $20.6 \pm 0.1$ | $0.030 \pm 0.001$ | $5.540 \pm 0.028$ | $9.10 \pm 0.03$ | $0.62 \pm 0.01$ | $2.21 \pm 0.02$ | $3.50 \pm 0.04$ | $4.25 \pm 0.04$ | |
| GHe-3 | $20.5 \pm 0.1$ | $0.030 \pm 0.001$ | $6.171 \pm 0.031$ | $10.08 \pm 0.04$ | $0.75 \pm 0.01$ | $2.64 \pm 0.05$ | $4.06 \pm 0.04$ | $4.72 \pm 0.05$ | |
| GHe-4 | $40.2 \pm 0.1$ | $0.051 \pm 0.001$ | $4.693 \pm 0.023$ | $7.88 \pm 0.05$ | $0.71 \pm 0.02$ | $2.20 \pm 0.04$ | $3.13 \pm 0.03$ | $3.50 \pm 0.05$ | $3.66 \pm 0.05$ |
| GHe-5 | $40.2 \pm 0.1$ | $0.051 \pm 0.001$ | $5.529 \pm 0.028$ | $9.29 \pm 0.07$ | $0.92 \pm 0.02$ | $2.70 \pm 0.04$ | $3.67 \pm 0.06$ | $4.17 \pm 0.05$ | |
| GHe-6 | $40.0 \pm 0.1$ | $0.051 \pm 0.001$ | $5.648 \pm 0.028$ | $9.45 \pm 0.07$ | $0.94 \pm 0.02$ | $2.76 \pm 0.05$ | $3.80 \pm 0.06$ | $4.25 \pm 0.08$ | |

compressed states could not be determined by only optical radiance from MCOP. In our experiments, the DPS application allowed for the measurement of the particle velocity at the He/LiF interface. The directly measured velocity by DPS is an apparent velocity, and the actual particle velocity should be corrected via the refractive index of the compressed LiF [28]. The corrected results are shown in Fig. 2(b), where the 1st step signal of DPS was analyzed to obtain the 1st shock particle velocity of LiF ($U_{p1,LiF}$). By the continuity condition at the He/LiF interface, the 2nd shock particle velocity ($U_{p2} = U_{p1,LiF}$) and the pressure ($P_2 = P_{1,LiF}$) of He could be deduced. In the data processing, the shock impedance of the foil approximately matched with that of LiF.

Successively, the multiple reverberation shock wave in the He chamber would transmit and impact the anvil again and again, where the shock breakout time at the He/LiF interface is shown in Fig. 2. In fact, the DPS signal reflects the multiple reverberation shock in the Al foil/LiF anvil interface. Due to the different shock velocity in the He chamber and Al foil, the deviation between the shock transmit time in He and the measured results by DPS have been considered. The time $t_2$, $t_3$, and $t_4$ mean the 2nd, 3rd, and 4th shock LiF anvil, respectively. So from the 2nd to the 4th step by DPS technique [see Fig. 2(b)] we can obtain the particle velocities of LiF including the 2nd, 3rd, and 4th shock compression. The multishock particle velocities of LiF are listed in Table I. In the continuity condition at the He/LiF interface, the corresponding particle velocity and the pressure of the 4th, 6th, and 8th shock He were determined. In order to obtain the whole multicompressed EOS of He, the shock states with odd numbers ($i = 3,5,7$) should be deduced by the shock transmitting time and the impedance matching at the He/driveplate interface. The similar detailed processing was illustrated in our previous work for argon [24]. After the 8th shock compression (partially 10th compression when the flyer impact velocity is slower, see Fig. 3), dense He would be compressed and approach the final equilibrium state. This can be observed from the highest steady flat of MCOP and DPS signal until the shock reached the sapphire interface.

Considering the EOS uncertainties under multiple compression, the main source of the uncertainty comes from the measurement error. Along with the multicompressed process, the uncertainty states of He could increase. From the 1st to the final compression, the pressure accuracy within $1\% \sim 10\%$ and density accuracy within $2\% \sim 20\%$ can be achieved. The integrated multiple compression states of He with different initial precompressed pressures of 20 MPa and 40 MPa are listed in Table II, where the experimental pressure-density ranges of 1–150 GPa and 0.1–1.1 g cm$^{-3}$ are presented. The typical results by the impedance matching solution are shown in Fig. 4.

In our work, multiple shock temperatures of He were extracted from the absolute spectral radiance of shock front [Fig. 2(a)] by using a gray body Planck radiation spectrum,

$$I(\lambda,T) = \varepsilon(T)\frac{2\pi hc^2}{\lambda^5}\left[\exp\left(\frac{hc}{\lambda k_B T}\right) - 1\right]^{-1}, \qquad (1)$$

where $T$ and $\lambda$ are the radiation temperature and the wavelength, $c$, $h$, and $k_B$ represent the speed of light, the Planck constant, and the Boltzmann constant, respectively, and $\varepsilon$ is the emissivity. Considering that current ionization degree is lower, the emissivity in our experimental state is regarded as a wavelength-independent function [13].

From the first nearly flat range of MCOP, the 1st shock spectral radiance was measured and the temperature ($T_1$) of single-shock He was obtained. Between the time $t_1$ and $t_2$, the reverberation shock passes through 2nd and 3rd compressed He sample, but the breakout between the 2nd and 3rd compression could not be distinguished by spectral radiance. This implies that dense He has become rather opaque after the 2nd compression. Though dense He under multiple

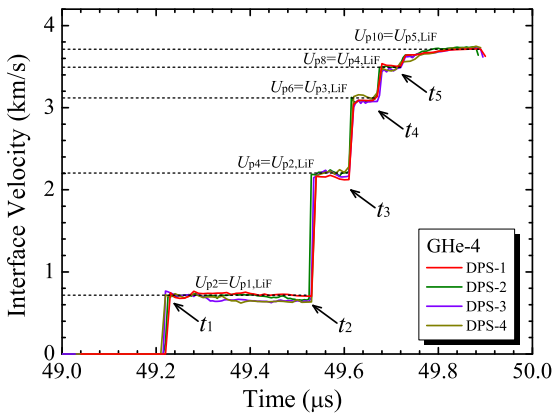


FIG. 3. The experimental signals of the He/LiF interface particle velocity history up to 10 times compression (the shot of No. GHe-4). The results are measured by a multichannel DPS technique. The signal amplitudes correspond to the particle velocities of the compressed sample He.

TABLE II. Multishock compression experimental EOS data for dense gaseous He. $P$, $\rho$, and $T$ are the pressure, the density, and the temperature in the He sample, respectively. The subscripts from 1 to 10 represent from single-shock to 10th-shock states, respectively.

| | | Multicompressed number | | | | | | | | | |
|---|---|---|---|---|---|---|---|---|---|---|---|
| Shot no. | States | 1st | 2nd | 3rd | 4th | 5th | 6th | 7th | 8th | 9th | 10th |
| GHe-1 | $P$ (GPa) | 1.53 ± 0.01 | 7.95 ± 0.09 | 22.60 ± 2.23 | 39.51 ± 1.10 | 62.60 ± 6.43 | 82.17 ± 2.88 | 96.24 ± 6.31 | 104.2 ± 5.03 | 109.9 ± 8.24 | 114.2 ± 7.09 |
| | $\rho$(g cm$^{-3}$) | 0.11 ± 0.01 | 0.25 ± 0.01 | 0.42 ± 0.02 | 0.62 ± 0.07 | 0.78 ± 0.10 | 0.86 ± 0.13 | 0.92 ± 0.14 | 0.95 ± 0.16 | 0.96 ± 0.16 | 0.96 ± 0.16 |
| | $T$ (kK) | 6.44 ± 0.20 | 10.60 ± 0.57 | 14.30 ± 0.61 | 16.70 ± 0.69 | 18.15 ± 0.67 | 18.60 ± 0.65 | 18.88 ± 0.63 | 19.03 ± 0.62 | 19.06 ± 0.62 | 19.07 ± 0.63 |
| GHe-2 | $P$ (GPa) | 1.86 ± 0.01 | 9.71 ± 0.11 | 26.31 ± 2.50 | 47.90 ± 1.40 | 77.34 ± 6.83 | 98.53 ± 3.63 | 115.3 ± 9.23 | 128.5 ± 6.49 | | |
| | $P$ (g cm$^{-3}$) | 0.12 ± 0.01 | 0.26 ± 0.01 | 0.47 ± 0.03 | 0.69 ± 0.07 | 0.86 ± 0.10 | 0.95 ± 0.14 | 1.01 ± 0.15 | 1.02 ± 0.16 | | |
| | $T$ (kK) | 8.51 ± 0.26 | 12.00 ± 0.62 | 15.80 ± 0.67 | 18.00 ± 0.70 | 19.72 ± 0.85 | 20.20 ± 0.96 | 20.57 ± 0.98 | 20.61 ± 0.99 | | |
| GHe-3 | $P$ (GPa) | 2.30 ± 0.01 | 12.20 ± 0.15 | 33.42 ± 2.91 | 60.29 ± 2.83 | 91.02 ± 6.37 | 117.3 ± 6.43 | 135.4 ± 10.3 | 152.9 ± 9.70 | | |
| | $\rho$ (g cm$^{-3}$) | 0.12 ± 0.01 | 0.27 ± 0.01 | 0.49 ± 0.03 | 0.70 ± 0.07 | 0.90 ± 0.11 | 0.99 ± 0.13 | 1.06 ± 0.14 | 1.06 ± 0.15 | | |
| | $T$ (kK) | 10.60 ± 0.40 | 16.60 ± 0.83 | 21.13 ± 0.95 | 23.00 ± 1.21 | 24.05 ± 1.55 | 24.30 ± 1.62 | 24.40 ± 1.66 | 24.42 ± 1.68 | | |
| GHe-4 | $P$ (GPa) | 2.30 ± 0.02 | 11.52 ± 0.34 | 27.41 ± 2.41 | 47.62 ± 3.06 | 68.66 ± 6.30 | 79.50 ± 5.45 | 89.26 ± 9.14 | 94.36 ± 8.09 | 98.98 ± 11.9 | 101.2 ± 10.8 |
| | $\rho$ (g cm$^{-3}$) | 0.18 ± 0.01 | 0.33 ± 0.02 | 0.54 ± 0.04 | 0.69 ± 0.07 | 0.79 ± 0.09 | 0.87 ± 0.13 | 0.92 ± 0.14 | 0.95 ± 0.17 | 0.96 ± 0.18 | 0.97 ± 0.18 |
| | $T$ (kK) | 4.60 ± 0.17 | 8.28 ± 0.25 | 13.40 ± 0.46 | 16.10 ± 0.54 | 17.76 ± 0.61 | 18.20 ± 0.64 | 18.48 ± 0.64 | 18.60 ± 0.65 | 18.68 ± 0.65 | 18.72 ± 0.66 |
| GHe-5 | $P$ (GPa) | 3.20 ± 0.03 | 15.43 ± 0.34 | 37.42 ± 3.10 | 61.98 ± 3.50 | 88.09 ± 7.11 | 102.8 ± 7.15 | 117.1 ± 12.8 | 124.4 ± 10.8 | | |
| | $\rho$ (g cm$^{-3}$) | 0.18 ± 0.01 | 0.36 ± 0.02 | 0.58 ± 0.04 | 0.76 ± 0.08 | 0.90 ± 0.10 | 1.00 ± 0.15 | 1.05 ± 0.17 | 1.07 ± 0.18 | | |
| | $T$ (kK) | 7.29 ± 0.12 | 11.80 ± 0.32 | 15.65 ± 0.35 | 17.50 ± 0.60 | 19.40 ± 0.78 | 20.50 ± 0.72 | 20.75 ± 0.88 | 20.90 ± 0.84 | | |
| GHe-6 | $P$ (GPa) | 3.33 ± 0.03 | 15.89 ± 0.37 | 39.21 ± 3.34 | 65.75 ± 4.30 | 91.38 ± 9.04 | 109.5 ± 8.75 | 121.5 ± 13.5 | 128.6 ± 13.8 | | |
| | $\rho$ (g cm$^{-3}$) | 0.18 ± 0.01 | 0.37 ± 0.02 | 0.61 ± 0.04 | 0.80 ± 0.09 | 0.95 ± 0.11 | 1.03 ± 0.16 | 1.08 ± 0.18 | 1.11 ± 0.20 | | |
| | $T$ (kK) | 7.80 ± 0.27 | 12.80 ± 0.48 | 17.62 ± 0.59 | 19.70 ± 0.60 | 20.60 ± 0.75 | 21.00 ± 0.75 | 21.25 ± 0.76 | 21.33 ± 0.78 | | |

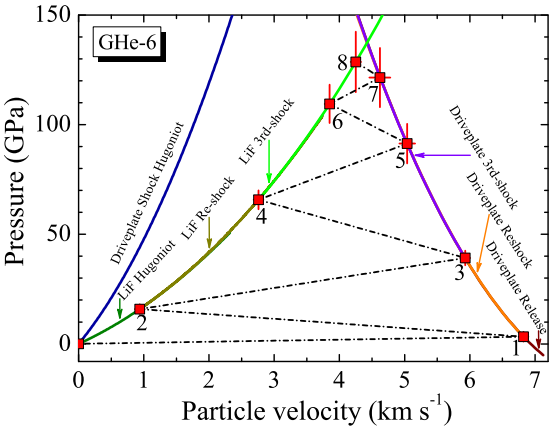


FIG. 4. Impedance matching solution to determine multiple compressed pressure and particle velocity for the shot of No. GHe-6. The solid red square symbols indicate the compressed states of current dense He.

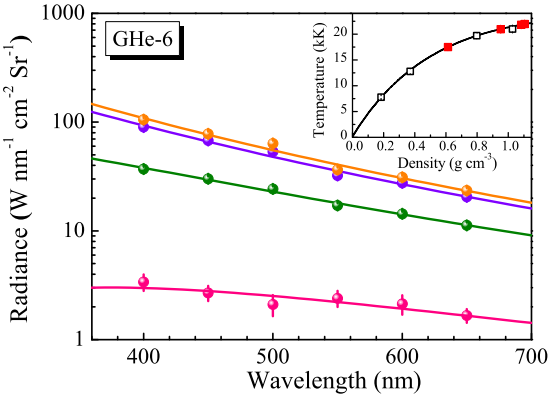


FIG. 5. Planck radiation fitting temperatures from the experimental spectral radiance under multiple shock compression for shot of No. GHe-6. The 1st (pink), 2nd (olive), 4th (violet), and 6th (orange) shocked radiances are listed. The colored solid curves are the corresponding Planck fitting results. Inset: The fitting temperatures (open squares) for the 1st, 2nd, 4th, and 6th shock compression are presented in the temperature-density plane. The 3rd, 5th, 7th, and 8th shock temperatures (red solid squares) were deduced by the interpolation and extrapolation method.

compression becomes opaque, the radiance from the He/LiF interface could be received by MCOP. For instance, the maximum intensity in the 2nd step range of MCOP reflects the 2nd shock spectral radiance. Subsequently, the He/LiF interface would be slightly destroyed due to the thermal ablation of LiF at high temperature, which results in an optical absorption and a decreasing radiance measurement. Along with the increase of the ablation layer thickness, the radiance would decrease gradually until the following shock anvil. In our data analysis, the absorption intensity is assumed independent with the wavelength, and this absorption effect would give no influence for the fitted temperature results. Successively, the 4th shock radiance and the 6th shock radiance could be determined from the maximum intensities in the 3rd and 4th steps separately. Therefore, the 2nd, 4th, and 6th shock temperatures could be obtained. By the interpolation and extrapolation method, the 3rd, 5th, 7th, and 8th shock temperatures were also deduced. Between the 3rd and 4th shock anvil the radiance increases, as shown in Fig. 2(a). In this region, the shock temperature changes very little and the shock transmission time is very short. Again, the shock thermal ablation in the He/LiF interface and the thermal conduction within the LiF anvil would have little influence on the radiance results. Figure 5 shows the typical experimental radiance fit for a shot of No. GHe-6, as well as the interpolation and extrapolation results in the temperature-density plane. Multishock temperature data in the range of 4600–24 000 K are listed in Table II.

## III. RESULTS AND DISCUSSION

In order to illustrate thermodynamic properties under multiple compression, the experimental $P$-$\rho$ data of dense He in our work are presented in Fig. 6. The cryogenic liquid He [10] and precompressed fluid He [29] both by gas gun, the corrected fluid He by laser and diamond anvil cell (DAC) [12], dense gaseous He quasi-isentropic [30], and the solid He isotherm [31] are also shown. As a whole, our experiments spread a wider P-$\rho$ regime of 1–150 GPa and 0.1–1.1 g cm$^{-3}$ with better uniformity. The data give an efficient offset in the pressure range of 20–50 GPa between the gas-gun and laser results. The wider compression ratio ($\eta_i = \rho_i/\rho_0$, $i$ = 1–8 and partially $i$ = 1–10, which are from the 1st to the 10th compressed states, respectively) were greatly improved from 3.5 to 43 based on the initial density ($\rho_0$). This can provide an important validation for the theoretical models. Different theoretical calculations for He by SVCH [17], ACTEX [18], DFT/PIMC [19], and Saha-He [30] are also shown in Fig. 6, where the former three models provided the principal Hugoniots of liquid He and the last one calculated the isentropic compression of gaseous He. The deviation among different Hugoniot calculations at higher pressure is obviously observed, and high-precision experiments are urgently required to constrain the EOS.

In our work, the experiments under multicompression pass through the Hugoniot curves and accord with the isentropic calculations by SAHA-He in higher pressure ranges. The partial results can be seen in Fig. 6 (inset) for one shot of No. GHe-6. The multiple compression curves from the corresponding states were calculated by self-consistent fluid variational theory (SFVT) [32,33]. In this shot the former three shocks belong to shock-adiabatic compression with the entropic addition ($S/R$ is from 12.9 to 13.4), and after that multicompression from the 4th to 8th compression is close to a quasi-isentropic process. This indicates what current multicompression would experience from shock-adiabatic to quasi-isentropic compression. Compared with the isentropic and isotherm results, multicompression technique can simultaneously achieve higher pressure and temperature in the same loading condition for the validation of EOS models.

Generally, the temperature data of He are indispensable in the phase diagram. It can provide an important validation for the theoretical models. Our experimental temperatures of He are presented in Fig. 7 to compare with previous experiments [13] and calculations [19,23,33–35] in the $P$-$\rho$-$T$ region, where the coupling parameter ($\Gamma$) is added to illustrate the WDM range. In the wider region, our experimental data from dense gaseous He give an efficient supplement for the EOS models. It

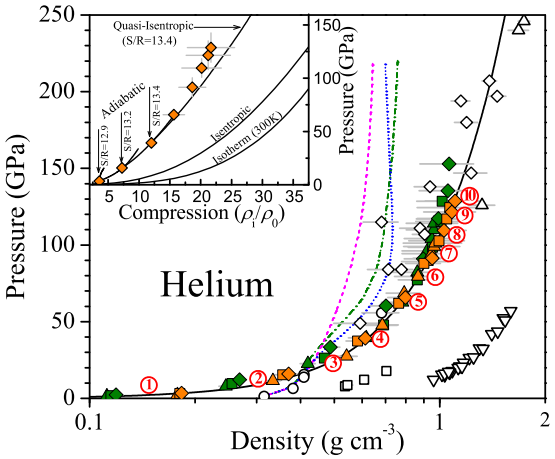


FIG. 6. Comparison of experimental and calculated EOS of He for different initial states. The colored symbols represent our experimental data from the 1st to 10th compression. The same color and symbol is for one shot. Our six-shots data are described as the olive triangles (GHe-1), olive squares (GHe-2), olive diamonds (GHe-3), orange triangles (GHe-4), orange squares (GHe-5), and orange diamonds (GHe-6), respectively. In comparison, the cryogenic liquid He [10] (open circles) and precompressed fluid He [29] (open squares) by gas gun, the corrected fluid He by laser and DAC [12] (open diamonds), dense gaseous He quasi-isentropic [30] (open triangles), and the solid He isotherm [31] (open inverted triangles) are also shown. Different models for liquid He by SVCH [17] (dash-dot olive), ACTEX [18] (blue dotted), DFT/PIMC [19] (dash-magenta), and SAHA-He [30] (solid black) are presented. Inset: Adiabatic to quasi-isentropic compression of dense He in our work is represented for the shot of GHe-6. The curves are calculated by SFVT.

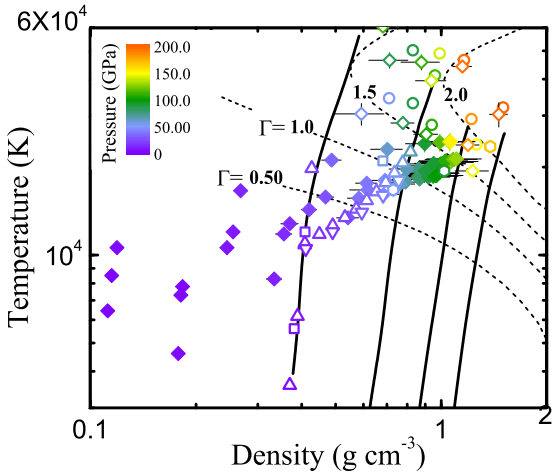


FIG. 7. Temperature-density plot of compressed He with experiments and calculations. Colors indicate pressure (inset scale). The experimental data: solid diamonds (our work) and open diamonds [13] with error bars. The calculated data: open squares [33], open triangles [35], open inverted triangles [19], open hexagons [23], and open circles [34]. The solid Hugoniot curves were calculated by DFT-MD [34] from the initially precompressed fluid He (precompression ratios are from 1 to 4). The coupling parameter (Γ) of He is added (dashed curves) to illustrate WDM range.

shows a good consistency with calculations by the free-energy model [35] and the DFT-MD model [19]. In higher density ranges, our multicompressed temperatures are lower than the results from the reflectivity experiments [13] and the DFT-MD calculations [34] in the approximate P and $\rho$ range. The reflectivity results and the DFT-MD calculations were deduced from the laser-driven shocks [11]. The sample He was statically precompressed by DAC to higher pressure, which was much higher than our initial states. By shock compression technique, our compression ratio and electron excitation and ionization would increase due to the decrease of the precompression density. The increased excitation and ionization would absorb the thermal energy in the system, which results in a lower temperature. In our multiple compression experiments, the coupling parameter in the range of $\Gamma > 1$ is obtained after the 4th compression, where our temperature-density range is beyond to ~18 kK and ~0.8 g cm$^{-3}$. That is to say, our experimental states above the 4th compression enter the WDM region.

In order to illustrate the successive compressibility of He under multiple compression, a comparison between the relative compression ratio ($\eta_i' = \rho_i/\rho_{i-1}$, $i$ = 1–10) and the pressure is presented in Fig. 8. In general, the shock compression ratio will become smaller if the sample is precompressed to higher density statically, which can be verified by our dense He with different initial pressures of 20 MPa and 40 MPa. For one shot under multiple compression, $\eta_i'$ gradually decreases with the increasing pressure due to the stronger repulsion interactions.

For different shots with the same compression number, $\eta_i'$ increases with pressure in the lower density regime and reversely decreases in the higher density regime. The turning points with a nonmonotonous relationship occur during the 3rd shock states for the initial precompressed pressure $P_0$ = 20 MPa and the 4th shock states for $P_0$ = 40 MPa, respectively. In this region the dense He was compressed to the pressure-density range of 30–70 GPa and 0.5–0.8 g cm$^{-3}$. The corresponding

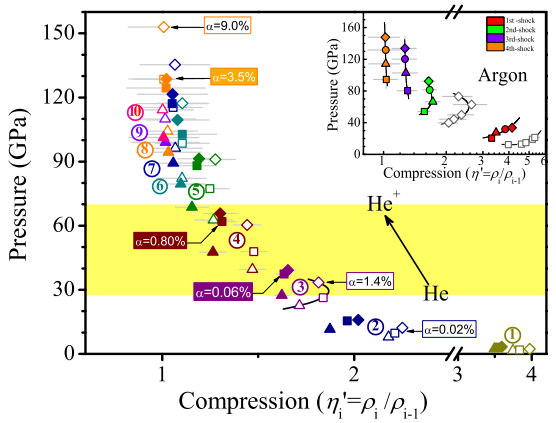


FIG. 8. Compressibility of multiple compressed dense He with different initial pressures of 20 MPa (solid) and 40 MPa (open). The same symbol is for one shot, and the same color means the same multicompression frequency. The solid curves are fitted from experimental data to describe the turning points at the same compression time. The ionization degrees ($\alpha$) of He were calculated by SFVT. The yellow region is shown for the turning points of relative compressibility. Inset: Multiple compression data of dense argon [24] is represented to illustrate the multishock compressibility.

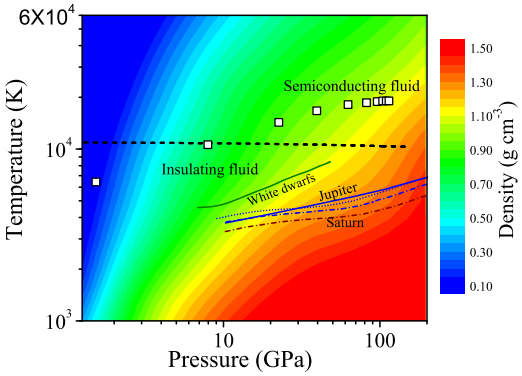


FIG. 9. Temperature-pressure-density contour of He fitted from the experiments and calculations. (The fitting data are from Fig. 7.) The phase boundary (dash-black curve) for fluid insulator–conductor He transformation [14] is presented. It indicates that our dense He (open squares, GHe-1) enters the semiconducting fluid region after the 2nd compression. For comparison, we show the interior isentropic conditions: the white dwarfs for effective temperatures of 6500 K by Saumon *et al.* [36] (solid olive); Jupiter by Saumon *et al.* [17] (solid blue), by Nettelmann *et al.* [21] (blue short-dotted), and by Militzer and Hubbard [3] (blue dash-dot); and Saturn by Militzer and Hubbard [3] (wine dash-dot).

ionization degree calculated by the SFVT model is from hardly any to 1%. This nonmonotonic evolution of the compression is controlled by two factors, where the excitation of internal degrees of freedom results in the increasing compressibility, and the repulsive interactions between the particles results in the decreasing compressibility at the onset of electron excitation and ionization. A similar phenomenon has been also observed in multicompressed argon [24]. In Fig. 8 with the increasing pressure and density, dense He would be compressed and approach the final equilibrium state with $\eta_i' \approx 1$ and the ionization is up to ~9% in our work.

Generally, the planetary and stellar interiors and atmospheres are described by the isentropic and homogeneous models, where Jupiter [3,17,21], Saturn [3], and white dwarf [36] isentropes are shown in Fig. 9. As the crucial component, dense He results are plotted in the $T$-$P$-$\rho$ contour of Fig. 9, which combines all the existing data of He EOS experiments and calculations. In the lower pressure and density range, the decrease of the density affects the sharp increase of the temperature. The temperature of He rises fast and the EOS results are mainly influenced by the thermal effect. In a higher pressure and density range, the rising temperature slows down and the compressed density increases gradually. This would strengthen the interaction of the particles and the density effect is dominant. In order to illustrate the conducting and optical properties under high pressure and temperature, Fig. 9 shows the insulating–conducting fluid transformation boundary of He [14], compared with our experimental results. It indicates that current warm dense He enters the partially conducting fluid region after the 2nd shock compression with a density-temperature of about 0.3 g cm$^{-3}$ and 1 eV. This is consistent with the opaque properties of dense helium and the strong absorption appearance after 2nd compression experiments. In these $T$ and $\rho$ regions, the conductivity ($\sigma$) was calculated by the simple semiconducting Drude model [13]. The estimated results show that our experiments enter a region with weak ionization ($\alpha < 1\%$) and semiconducting fluid [$\sigma_{DC} \approx 10^4\,(\Omega\,\mathrm{m})^{-1}$]. The ionization degree and the free electron are poor, and the optical transformation was explained by the electrons of low mobility in an amorphous semiconductor [14]. Therefore the experimental results of dense He can provide the reference validation for white dwarf atmospheres with opaque dense He and the planetary interior structure and evolution models.

## IV. CONCLUSION

In our work, dense gaseous He has been compressed to a warm dense region from shock-adiabatic to quasi-isentropic compression paths. By means of an elaborate target design, the multicompressed experimental $P$-$\rho$-$T$ states in the 1-Mbar range were measured to constrain the EOS models. The optical radiance measurement shows that dense He becomes opaque after the 2nd compression. It implies that dense He transforms from optically transparent insulators to opaque semiconducting fluid under multiple compression. This has a reference value for the white dwarf stars with unexpectedly opaque He atmospheres. Under multiple compression, thermodynamic properties and compressibility of warm dense He was developed. Current experimental results and the opacity of dense He can provide the reference proof for the structure and evolution of planetary models. Our experimental target design and the diagnostic techniques can be applied to other warm dense matter, such as mixtures of hydrogen and helium, and detonation products.

## ACKNOWLEDGMENTS

We would thank our colleagues for the gas-gun operation, experimental diagnosis, and devices. Our work was supported by the National Natural Science Foundation of China (Grants No. 11504352, No. 11674292, and No. 11604315), the Presidential Foundation of CAEP (Grant No. 201501032), the CAEP Foundation (Grant No. 2015B0102001), the Science Challenge Project (Grant No. TZ2016001), the LSD Foundation (Grant No. 9140C670103150C67289), and the Foundation of Laboratory of Pulsed Power (Grant No. PPLF2016PZ04).

[1] M. D. Knudson, M. P. Desjarlais, A. Becker, R. W. Lemke, K. R. Cochrane, M. E. Savage, D. E. Bliss, T. R. Mattsson, and R. Redmer, Direct observation of an abrupt insulator-to-metal transition in dense liquid deuterium, Science **348**, 1455 (2015).

[2] L. B. Fletcher, H. J. Lee, T. Doppner, E. Galtier, B. Nagler, P. Heimann, C. Fortmann, S. LePage, T. Ma, M. Millot *et al.*, Ultrabright x-ray laser scattering for dynamic warm dense matter physics, Nat. Photon. **9**, 274 (2015).

[3] B. Militzer and W. B. Hubbard, Ab initio equation of state for hydrogen-helium mixtures with recalibration of the giant-planet mass-radius relation, Astrophys. J. **774**, 148 (2013).

[4] J. Y. Dai, D. D. Kang, Z. X. Zhao, Y. Q. Wu, and J. M. Yuan, Dynamic Ionic Clusters with Flowing Electron Bubbles from Warm to Hot Dense Iron along the Hugoniot Curve, Phys. Rev. Lett. **109**, 175701 (2012).

[5] K. P. Driver and B. Militzer, All-Electron Path Integral Monte Carlo Simulations of Warm Dense Matter: Application to Water and Carbon Plasmas, Phys. Rev. Lett. **108**, 115502 (2012).

[6] S. X. Hu, L. A. Collins, T. R. Boehly, J. D. Kress, V. N. Goncharov, and S. Skupsky, First-principles thermal conductivity of warm-dense deuterium plasmas for inertial confinement fusion applications, Phys. Rev. E **89**, 043105 (2014).

[7] F. Graziani, M. P. Desjarlais, R. Redmer, and S. B. Trickey, *Frontiers and Challengers in Warm Dense Matter* (Springer International Publishing, Switzerland, 2014).

[8] J. J. Barnard, R. J. Briggs, D. A. Callahan, R. C. Davidson, A. Friedman, L. Grisham, E. P. Lee, R. W. Lee, B. G. Logan, C. L. Olson *et al.*, Accelerator and ion beam tradeoffs for studies of warm dense matter, in *Proceedings of the 2005 Particle Accelerator Conference, Knoxville, Tennessee* (IEEE, New York, 2005), pp. 2568–2570.

[9] F. Soubiran, S. Mazevet, C. Winisdoerffer, and G. Chabrier, Helium gap in the warm dense matter regime and experimental reflectivity measurements, Phys. Rev. B **86**, 115102 (2012).

[10] W. J. Nellis, N. C. Holmes, A. C. Mitchell, R. J. Trainor, G. K. Governo, M. Ross, and D. A. Young, Shock Compression of Liquid Helium to 56 GPa (560 kbar), Phys. Rev. Lett. **53**, 1248 (1984).

[11] J. Eggert, S. Brygoo, P. Loubeyre, R. S. McWilliams, P. M. Celliers, D. G. Hicks, T. R. Boehly, R. Jeanloz, and G. W. Collins, Hugoniot Data for Helium in the Ionization Regime, Phys. Rev. Lett. **100**, 124503 (2008).

[12] S. Brygoo, M. Millot, P. Loubeyre, A. E. Lazicki, S. Hamel, T. T. Qi, P. M. Celliers, F. Coppari, J. H. Eggert, D. E. Fratzunduono *et al.*, Analysis of laser shock experiments on precompressed samples using a quartz reference and application to warm dense hydrogen and helium, J. Appl. Phys. **118**, 195901 (2015).

[13] P. M. Celliers, P. Loubeyre, J. H. Eggert, S. Brygoo, R. S. McWilliams, D. G. Hicks, T. R. Boehly, R. Jeanloz, and G. W. Collins, Insulator-to-Conducting Transition in Dense Fluid Helium, Phys. Rev. Lett. **104**, 184503 (2010).

[14] R. S. McWilliams, D. A. Dalton, Z. Konopkova, M. F. Mahmood, and A. F. Goncharov, Opacity and conductivity measurements in noble gases at conditions of planetary and stellar interiors, Proc. Natl. Acad. Sci. USA **112**, 7925 (2015).

[15] V. E. Fortov, V. Ya. Ternovoi, M. V. Zhernokletov, M. A. Mochalov, A. L. Mikhailov, A. S. Filimonov, A. A. Pyalling, V. B. Mintsev, V. K. Gryaznov, and I. L. Iosilevskii, Pressure-produced ionization of nonideal plasma in a megabar range of dynamic pressures, JETP **97**, 259 (2003).

[16] M. A. Mochalov, R. I. Ilkaev, V. E. Fortov, A. L. Mikhailov, V. A. Arinin, A. O. Blikov, A. Yu. Baurin, V. A. Komrakov, V. A. Ogorodnikov, A. V. Ryzhkov, and A. A. Yukhimchuk, Measurement of the quasi-isentropic compressibility of a helium plasma at a pressure of about 5000 GPa, JETP Lett. **96**, 158 (2012).

[17] D. Saumon, G. Chabrier, and H. M. Van Horn, An equation of state for low-mass stars and giant planets, Astrophys. J. Suppl. Ser. **99**, 713 (1995).

[18] M. Ross, F. Rogers, N. Winter, and G. Collins, Activity expansion calculation of shock-compressed helium: The liquid Hugoniot, Phys. Rev. B **76**, 020502(R) (2007).

[19] B. Militzer, First Principles Calculations of Shock Compressed Fluid Helium, Phys. Rev. Lett. **97**, 175501 (2006).

[20] W. Lorenzen, B. Holst, and R. Redmer, Demixing of Hydrogen and Helium at Megabar Pressures, Phys. Rev. Lett. **102**, 115701 (2009).

[21] N. Nettelmann, A. Becker, B. Holst, and R. Redmer, Jupiter models with improved ab initio hydrogen equation of state (H-REOS.2), Astrophys. J. **750**, 52 (2012).

[22] A. Forster, T. Kahlbaum, and W. Ebeling, Equation of state and the phase diagram of dense fluid helium in the region of partial ionization, Laser Part. Beams **10**, 253 (1992).

[23] A. Kietzmann, B. Holst, R. Redmer, M. P. Desjarlais, and T. R. Mattsson, Quantum Molecular Dynamics Simulations for the Nonmetal-to-Metal Transition in Fluid Helium, Phys. Rev. Lett. **98**, 190602 (2007).

[24] J. Zheng, Q. F. Chen, Y. J. Gu, Z. G. Li, and Z. J. Shen, Multishock compression properties of warm dense argon, Sci. Rep. **5**, 16041 (2015).

[25] N. C. Holmes, M. Ross, and W. J. Nellis, Temperature measurements and dissociation of shock-compressed liquid deuterium and hydrogen, Phys. Rev. B **52**, 15835 (1995).

[26] J. D. Weng, H. Tan, X. Wang, Y. Ma, S. L. Hu, and X. S. Wang, Optical-fiber interferometer for velocity measurements with picoseconds resolution, Appl. Phys. Lett. **89**, 111101 (2006).

[27] T. S. Duffy and T. J. Ahrens, Dynamic compression of an Fe–Cr–Ni alloy to 80 GPa, J. Appl. Phys. **82**, 4259 (1997).

[28] Z. G. Li, Q. F. Chen, Y. J. Gu, J. Zheng, and X. R. Chen, Measurements of the principal Hugoniots of dense gaseous deuterium−helium mixtures: Combined multi-channel optical pyrometry, velocity interferometry, and streak optical pyrometry measurements, AIP Adv. **6**, 105309 (2016).

[29] C. T. Seagle, W. D. Reinhart, A. J. Lopez, R. J. Hickman, and T. F. Thornhill III, High precision Hugoniot measurements on statically pre-compressed fluid helium, J. Appl. Phys. **120**, 125902 (2016).

[30] M. V. Zhernokletov, V. K. Gryaznov, V. A. Arinin, V. N. Buzin, N. B. Davydov, R. I. Ilkaev, I. L. Iosilevskiy, A. L. Mikhailov, M. G. Novikov, V. V. Khrustalev, and V. E. Fortov, Quasi-isentropic compression of dense gaseous helium at pressures up to 500 GPa, JETP Lett. **96**, 432 (2012).

[31] P. Loubeyre, R. LeToullec, J. P. Pinceaux, H. K. Mao, J. Hu, and R. J. Hemley, Equation of State and Phase Diagram of Solid $^4$He from Single-Crystal X-Ray Diffraction over a Large P-T Domain, Phys. Rev. Lett. **71**, 2272 (1993).

[32] Q. F. Chen, L. C. Cai, Y. J. Gu, and Y. Gu, Ionization and equation of state of dense xenon at high pressures and high temperatures, Phys. Rev. E **79**, 016409 (2009).

[33] Q. F. Chen, Y. Zhang, L. C. Cai, Y. J. Gu, and F. Q. Jing, Self-consistent variational calculation of the dense fluid helium in the region of partial ionization, Phys. Plasmas **14**, 012703 (2007).

[34] B. Militzer, Path integral Monte Carlo and density functional molecular dynamics simulations of hot, dense helium, Phys. Rev. B **79**, 155105 (2009).

[35] J. M. Aparicio and G. Chabrier, Free-energy model for fluid atomic helium at high density, Phys. Rev. E **50**, 4948 (1994).

[36] P. Bergeron, D. Saumon, and F. Wesemael, New model atmospheres for very cool white-dwarfs with mixed H/He and pure He compositions, Astrophys. J. **443**, 764 (1995).